Elastic constants of nano-scale hydrated cement paste composites using reactive molecular dynamics simulations to homogenization of hardened cement paste mechanical properties

Sela Hoeun, Fabrice Bernard, Frederic Grondin, Siham Kamali-Bernard, Syed Yasir Alam

Elastic constants of nano-scale hydrated cement paste composites using reactive molecular dynamics simulations to homogenization of hardened cement paste mechanical properties

Sela Hoeun[1,2], Fabrice Bernard[2], Frédéric Grondin[1], Siham Kamali-Bernard[2], Syed Yasir Alam[1]

[1] Institut de Recherche en Génie Civil et Mécanique (GeM), UMR 6183 Centrale Nantes – Université de Nantes – CNRS, 1 rue de la Noë 44321 Nantes cedex 3, France

[2] Laboratoire de Génie Civil et Génie Mécanique (LGCGM), University of Rennes, INSA Rennes, 20 avenue des Buttes de Coësmes 35700 Rennes, France

Keywords: Elastic constants, hydrated cement paste phases, molecular dynamics, homogenization, Reuss-Voigt-Hill approximation, Young's modulus

Abstract

Calcium-silicate-hydrates, portlandite and ettringite are the main hydrated cement paste phases. The study of these phases might lead to a better understanding of the mechanical properties of hardened cement paste. In this work, molecular dynamics simulations were used to simulate different composites of these main phases. The objective were to obtain their elastic constants and to use them as a reference to calculate the homogenization of simplified hardened cement paste using Mori-Tanaka scheme. The results of calcium-silicate-hydrate/calcium-silicate-hydrate, calcium-silicate-hydrate/portlandite and calcium-silicate-hydrate/ettringite composites with three different orientations and configurations were obtained via molecular dynamics

simulations using a software called LAMMPS. The homogenization of simplified hardened Portland cement paste gave the value of Young's modulus in the range from 10.1 GPa to 15.1 GPa. This method might be able to determine Young's modulus of normal hardened cement paste by the calculations of elastic constants of different composites with other hydrated and unhydrated phases.

1. Introduction

Cementitious materials are by far the most used materials that are characterized by a heterogeneous composition on several scales. Due to this complex structure, the behavior of concrete and especially its cracking remain relatively controlled. Concrete is composed of aggregates (a particulate phase) and cement matrix (a binding phase) as a complex composite. Consequently, the cement matrix influences the mechanical properties of concrete [1,2]. Cement paste is a porous multiscale substance with various physical properties at varying length scales [3]. Calcium-silicate-hydrate (C-S-H) representing at least 50% of the volume is the major component of hardened hydrated cement paste [2]. In hydrated Portland cement paste, another considerable phase is portlandite (CH). For pastes of typical Portland cements cured for 3-12 months, the portlandite content found by thermal methods or QXDA is typically 15-25%, referred to the ignited mass [4]. In addition, another hydration product of Portland, more particularly slag and super-sulphated cements but not only, is ettringite which is an important phase to be considered particularly in durability aspects [5].

In order to simulate accurately the behavior of the concrete, it is important to develop the finest possible modeling of the cement paste and to ascend to the overall behavior of

the cement-based composite material. The chemistry and fineness of the cement, quantity of water, ratio of additives and admixtures, mixing method, and temperature have a significant impact on the paste's properties. Therefore, any attempt to simulate concrete without accounting for the heterogeneity of the cement paste requires systematic calibration of the latter's mechanical properties, for instance by experimental tests. This hinders the advancement of novel concrete made from industrial by-product (i.e., green-concrete).

The multi-scale modeling requires the mechanical properties of different phases of cement paste. One of the method to obtain those properties is using nano-indentation experiments [6]. However, uncertainties from the lowest scale conduct to no negligible uncertainties at concrete scale and induce the use of security factors and overestimation of structure. The characterization of the nanoscale structure of cement-based materials and breakthroughs in computational materials science have made it possible for scientists and engineers to well understand and design concrete, as well as to increase its durability and performance. In civil engineering, numerous analytical and/or numerical modeling works taking heterogeneity into account have thus been gradually published [1,6–14]. However, it is the rupture of the adhesion between these phases which is responsible for the damage of the material and the micro-cracking even more than the rupture of the phases themselves (inter-phase and not intra-phase ruptures) [15–18].

Thus, this paper describes the method to obtain the mechanical properties of the phase itself and the composite phases between different main cement paste phases using molecular dynamics (MD) simulations. This includes the calculation of the elastic

constants, Young's moduli and Poisson's ratios via Voigt-Reuss-Hill (VRH) approximation, and finally using the homogenization scheme (i.e., Mori-Tanaka scheme) to calculate Poisson's ratios and Young's moduli of simplified hardened cement paste (HCP). This method expects to predict the elastic properties with a minimum of uncertainties.

The paper is divided into three main sections. Section 2 describes materials and methods including microstructure of hydrated cement, molecular dynamics and LAMMPS, force field, and simulation procedure. Section 3 provides results and discussion related to elastic constants, Young's moduli and Poisson's ratios and homogenization of simplified HCP. Finally, section 4 will show the conclusion of this study.

2. Materials and Methods

2.1. Microstructure of hydrated cement

Hydration of Portland cement creates different hydration products including amorphous or poorly crystalline C-S-H and coarsely CH. For example, from a case of 14 months saturated old Portland cement paste with water-to-cement (w/c) ratio of 0.5 , Taylor [4] calculated volume percentages based on the phase composition to be: C-S-H = 48.7%, CH = 13.9%, AFt = 3.6%, Alite = 1%, Belite = 0.6%, Ferrite = 1%, AFm = 11.1%, Hydrogarnet = 2.2%, Hydrotalcite = 1.8%, insoluble residue = 1%, and pores = 16%. In relation to the volume percentages of phase composition, three primary phases were selected to study (i.e., C-S-H, CH and AFt).

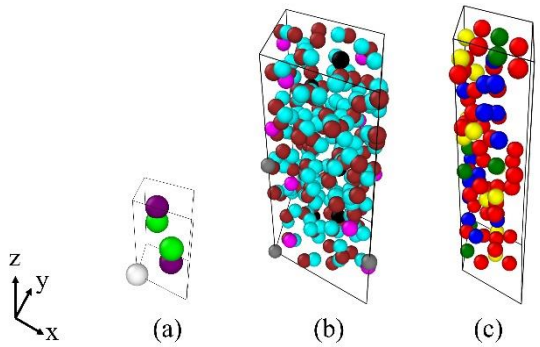

Fig. 1. Unit cells of calcium hydroxide, ettringite and tobermorite 11 Å in perspective view: (a) in CH phase, white balls are Ca atoms, lime balls are H atoms, and purple balls are O atoms, (b) in ettringite phase, gray balls are Al atoms, magenta balls are Ca atoms, cyan balls are H atoms, brown balls are O atoms, and black balls are S atoms, and (c) in tobermorite 11 Å phase, green balls are Ca atoms, yellow balls are Si atoms, red balls are O atoms, and blue balls are H atoms.

The formation of CH always occurs in conjunction with the hydration of C_3S or C_2S. In the hydration of C_3S paste, the majority of CH precipitates as portlandite crystals, some of which can reach tens of micrometers in diameter [19]. CH has a trigonal space group ($P\bar{3}m1$) with cell lengths of a = b = 3.589 Å and c = 4.911 Å at room temperature. It has cell angles (α, β, γ) = (90^0, 90^0, 120^0) and chemical formula $Ca(OH)_2$. The CH unit cell was modelled following Desgranges et al. [20] as shown in **Fig. 1a**.

The general formula for ettringite is $[Ca_3(Al,Fe)(OH)_6]X_3 \cdot xH_2O$, where X is a formula unit for a doubly charged anion. Ettringite is a member of the large group of AFt phases. At the nanometer scale, ettringite is composed of columns of the chemical formula $[Ca_3Al(OH)_6 \cdot 12H_2O]^{26-}$ that are parallel to the c-axis, with $3SO_4^{2-}$ and H_2O molecules in the channels in between [19]. The ettringite (AFt) unit cell at 23 °C was modelled following Goetz-Neunhoeffer and Neubauer [21] with cell angles $\alpha = 90^0$, $\beta =$

90^0, $\gamma = 120^0$, cell lengths (a, b, c) = (11.229 Å, 11.229 Å , 21.478 Å) and chemical formula $Ca_6[Al_2(SO_4)_3(OH)_{12}]\cdot 26H_2O$ as shown in **Fig. 1b**.

Amorphous or nearly amorphous C-S-H products are referred as the 'C-S-H phase.' At room temperature, hydration of C_3S produces C-S-H phase, which appears to be structurally related to the crystalline phases of 1.1 nm tobermorite and jennite as well as to the weakly crystalline substances C-S-H (I) and C-S-H (II) [19]. The structure of the semi-crystalline phase C-S-H (I), which can be made by mixing sodium silicate solutions with calcium salt solutions or by reacting calcium hydroxide with hydrous silica, is comparable to that of tobermorite at short-range length scale. It can be made with a Ca/Si molar ratio of between about 0.8 and 1.5. Similar in short-range structure to jennite, the phase C-S-H (II) may be created by hydrating C_3S or β-C_2S in excess water and repeatedly draining the liquid to reduce the CaO/SiO_2 ratio in the system [19]. One possible ordered of the structures of 11 Å natural tobermorite is a monoclinic crystal system $P2_1$ with cell lengths (a, b, c) = (6.69 Å, 7.39 Å, 22.779 Å), cell angle $\gamma = 123.49^0$ and chemical formula ($Ca_4Si_6O_{14}(OH)_4\cdot 2H_2O$) as shown in **Fig. 1c** [22]. Fu [23] developed C-S-H cell, which long range was distorted, initially from tobermorite 11 Å and acquired the first amorphous tobermorite. We got the annealed amorphous structure, which is C-S-H (I) with the Ca/Si ratio of 0.67, following his methodology.

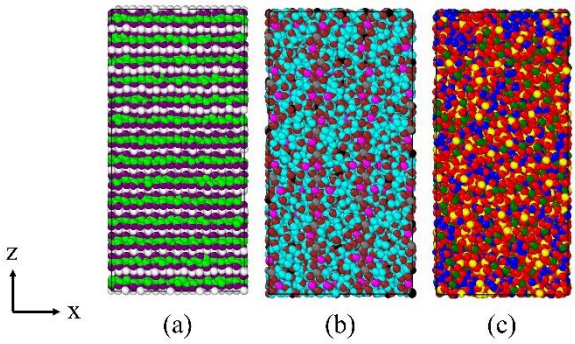

Fig. 2. Supercells of calcium hydroxide, ettringite and C-S-H (I) after relaxation with NPT ensemble in xz plan: (a) supercell of 9×10×14 CH, (b) supercell of 3×3×3 AFt, and (c) supercell of 5×5×3 C-S-H (I).

As shown in **Fig. 2**, CH was replicated 9 times in x-direction, 10 times in y-direction, and 14 times in z-direction to get a larger cell (i.e., supercell CH). Ettringite and C-S-H (I) were likewise replicated 3×3×3 and 5×5×3 times in x-, y-, and z-directions, respectively. The replicated cells are called supercell AFt and C-S-H (I). The sizes of supercells were chosen to ensure that sizes of all chosen phases in three dimensions are approximately similar. We have chosen ettringite as the reference because its unit cell is the largest in all three dimensions. It means that this way makes it easier to replicate other phases to have similar dimensions. All colors of balls, which represent different types of atoms, remain the same in this paper.

2.2. Molecular dynamics and LAMMPS

A method for calculating equilibrium and transport characteristics of a classical many-body system is called molecular dynamics simulations. The term "classical" in this regard refers to the fact that nuclear motion of constituent particles complies with laws of classical mechanics. For many different types of materials, this is a great

approximation [24]. MD simulations and actual experiments are remarkably similar in many ways. In experimental tests, one carries out the following steps. A sample of the content ones intends to investigate is prepared. One attaches this sample to a measuring device (such as a manometer, thermometer, or viscometer), and then one measures the desired property for a predetermined period. Similar strategy was employed in MD simulations [24].

Large-scale Atomic/Molecular Massively Parallel Simulator is what LAMMPS stands for. Since the release of open source code of classical molecular dynamics simulator LAMMPS in 2004, it has gained popularity as a tool for particle-based modeling of materials at length scales varying from continuum to mesoscale to atomic. There are several reasons for its popularity. Firstly, it provides a wide range of particle interaction models for various materials. Secondly, it is the fact that it runs on all platforms from single CPU cores to the largest supercomputers with accelerators. Lastly, it gives users control over simulation details through the input script or by adding code for new interatomic potentials, constraints, diagnostics, or other features required for their models [25].

2.3. Force field

Force field is quite important in MD simulations and there are multiple force fields (e.g., Clay Force Field (ClayFF) [26] which is a Classical MD and Reactive Force Field (ReaxFF) [27] which is a Reactive MD). For ClayFF, it is compatible with CH and C-S-H, whereas ReaxFF could be used with CH, C-S-H and sulfoaluminate (AFm or AFt). In order to run ClayFF in LAMMPS, bonds between atoms are created at the beginning

of the simulation. For ReaxFF, it is not required to create bonds between atoms at the start of simulation. Hence, it fits to model the composite between main cement paste phases, in particular the interaction at the interface. However, ReaxFF is time consuming compared to ClayFF.

In order to create a practical MD simulation of large scale reactive chemical systems, Van Duin et al. [27] developed ReaxFF for Hydrocarbons, which is a force field for reactive systems. ReaxFF utilized a general relationship between bond distance and bond order. Furthermore, it employed a general relationship between bond energy and bond order that led to proper dissociation of bonds in order to separate atoms. Other valence terms that presented in force field (angle and torsion) were defined in terms of same bond orders. Consequently, all these terms moved smoothly to zero as the bond break. In addition, Morse (van der Waals) and Coulomb potentials were also composed in ReaxFF in order to describe non-bonded interactions between all atoms. The classical force fields were unable to characterize the chemical reactions that will be triggered by large deformations. Via Reactive Molecular Dynamics simulations using ReaxFF, this matter has been taken into account in the study of Hajilar and Shafei [28]. The classical MD harmonic bonds were replaced by bond orders and energies upon the interatomic distances. While the bonded interactions were allowed to decay smoothly to zero, it could capture the bond breakage and formation with this approach. Such an approach has already been used in [29] for other cement nanocomposites and presented thus many advantages compared to the Classical Molecular Dynamics simulations for which constructions of model were more difficult [30,31].

For all atoms in system using a screened taper function, the van der Waals and non-bonded Columbic interactions were obtained. The charged equilibrium (Q_{Eq}) method set the atomic charges and was required to be updated at each time step. ReaxFF parameters could be found in Liu et al. [32]. ReaxFF separated the system energy up to different partial energy contributions as shown in **Eq. (1)** comparable to the empirical non-reactive force fields [27].

$$E_{system} = E_{bond} + E_{over} + E_{under} + E_{val} + E_{pen} + E_{tor} + E_{conj} + E_{vdW} + E_{coul} \quad (1)$$

where E_{bond} is bond energy, E_{over} and E_{under} are energy penalty for over- and under-coordination of atoms, E_{val} E_{pen} E_{tor} E_{conj} E_{vdW} and E_{coul} are valence angle, penalty, torsion, conjugation, Van der Waals and Coulombic energy, respectively.

2.4. Simulation procedure

Several points will be discussed in this section. Those are elastic constants calculation via MD simulations, Young's modulus (E) and Poisson's ratio (ν) obtained from VRH approximation, and utilization of homogenization scheme (i.e., Mori-Tanaka scheme) to obtain E and ν of the simplified hardened cement paste.

2.4.1. Model construction

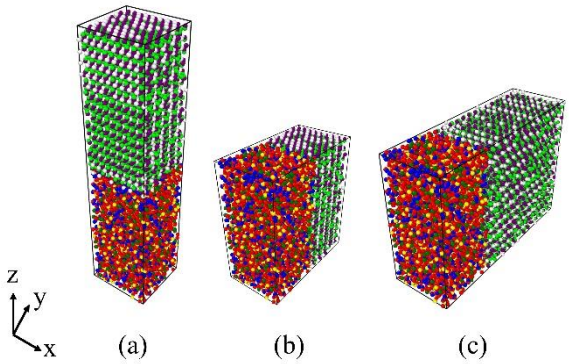

Fig. 3. Orientation of model construction of C-S-H (I)/CH: (a) CH supercell was placed on top of C-S-H (I) supercell in z-direction, (b) CH supercell was placed on the side of C-S-H (I) supercell in y-direction, and (c) counterclockwise rotated CH supercell around x-axis in yz plan was placed on the side of CH supercell in y-direction.

In the work of Liang [33], the unit cells of C-S-H and CH were replicated in order to get the believable results. Then the supercells were relaxed individually with NPT ensemble at 300 K and 0 Pa at x-, y- and z-directions. The relaxed supercells were placed together with the gaps of about 3 Å at the interface and relaxed again with NPT ensemble. These procedures are similar. Firstly, unit cells were replicated in x-, y- and z-directions, respectively. The simulation was modelled in 3D in LAMMPS with periodic boundary condition (PPP). Then they were changed to orthogonal cells to get independent results to each direction since unit cells of CH and AFt have trigonal space groups, and unit cell of C-S-H (I) has a monoclinic space group. The supercells were applied under energy minimization and relaxation with NPT ensemble for 50 ps with pressure of 0 atm and temperature of 300 K in x-, y- and z-directions. Finally, composite of different phases were constructed by placing supercell together following the same steps. It means that composite was applied again under energy minimization and relaxation with

NPT ensemble for 50 ps with pressure of 0 atm and temperature of 300 K in x-, y- and z-directions.

Three orientations were decided due to the fact that Bonnaud et al. [34] studied three various orientation configurations of C-S-H particle pairs employed to investigate the interaction grand potential at the molecular level. They chose these orientations to take into account the effects of: (a) anisotropic in crystallography and geometry of C-S-H particles, and (b) different interaction forces among particles related to orientation. In addition, they moved the other particle to compute the interaction grand potentials at different interparticle distance. They found different interparticle distances related to the minimum interaction grand potential minima. Subsequently, vacuum and different water spacing were imposed between supercells in our study. Zhu et al. [35] studied the hydrated surface properties of C-S-H via MD simulations and ReaxFF force field. They used SPC/E water model in their simulation. As a result, SPC/E water model was employed to model the 3.1 Å and 6.2 Å water spacing in this paper. We have done three distinct orientations for composites: (a) supercell CH on top of supercell C-S-H (I) in z-direction, (b) supercell CH on the side of supercell C-S-H (I) in y-direction, and (c) counterclockwise rotated supercell CH around x-axis on the side of supercell C-S-H (I) in y-direction as shown in **Fig. 3**. It should be noticed that in order to have a similar dimension in y-direction for the counterclockwise rotated case, the supercells of CH and AFt were replicated to 9×22×14 and 3×7×3 in x-, y-, and z-directions, respectively. Then, these supercells were counterclockwise rotated around x-axis in yz plan where bottom of these supercells were placed to the side of C-S-H (I) supercell. As could be seen in **Fig. 4**, there are three different configurations: (a) 1 Å vacuum spacing was

placed between supercell C-S-H (I) and CH, (b) 3.1 Å water spacing was placed between supercell C-S-H (I) and CH, and (c) 6.2 Å water spacing was placed between supercell C-S-H (I) and CH.

By way of comparison, the equilibrium distance between two C-S-H globules that can be calculated from Bonnaud et al.'s results [34] is approximately comprised in between 2 and 4 nm. Distances between supercells that exceed this range of values have been deliberately considered. Note that distance of 3.1 Å is located exactly in the middle of values identified by Bonnaud et al. [34].

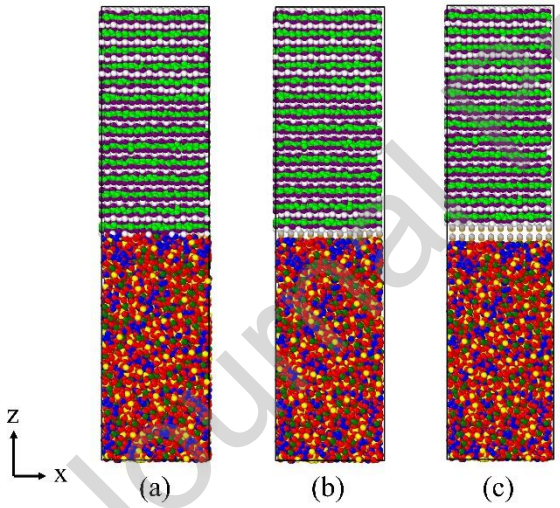

Fig. 4. Model construction of composite: (a) C-S-H (I)/vacuum (1 Å)/CH composite, (b) C-S-H (I)/H_2O (3.1 Å)/CH composite, and (c) C-S-H (I)/H_2O (6.2 Å)/CH composite in z-direction. In water layer between two supercells, silver balls are H atoms, and orange balls are O atoms.

2.4.2. Elastic constants calculation and VRH approximation

Eftekhari and Mohammadi [36] investigated on the numerical study of enhanced mechanical properties of C-S-H reinforced using the embedded carbon nanotube (CNT)

in its molecular structure. The uniaxial and shear deformations were introduced in six independent directions (axial x, y, z and shear xy, xz, yz) of the simulation box with a constant velocity of 1 Å/ps in an NVT ensemble after the system was in the equilibrium state. From applied strain, pressure of the system was obtained. Accordingly, the corresponding stress-strain response was acquired once the full application of deformation is reached. Then, they calculated the elastic constants of the models from the initial linear part of the obtained stress-strain curves.

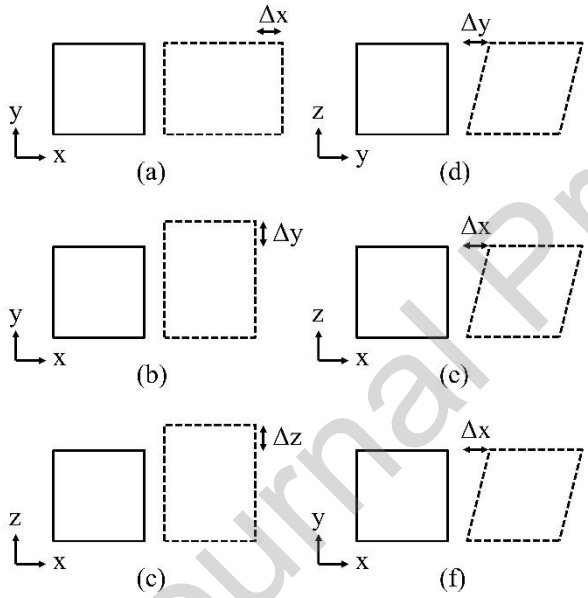

Fig. 5. Six deformation directions: (a) tensile in x-direction, (b) tensile in y-direction, (c) tensile in z-direction, (d) shear in yz-direction, (e) shear in xz-direction, and (f) shear in xy-direction.

In our study, deformations on six different directions were performed once at a time as shown in **Fig. 5** while relaxing with NPT (temperature of 300 K and pressure of 0 atm) in directions whose values of elastic constants equaled to zero. For example, in the space group of trigonal, C_{51} and C_{61} are equaled to zero. Thus, we relaxed with NPT ensemble in xz- and xy- directions. **Fig. 6** shows deformation in z-direction with the C-

S-H (I)/H_2O (6.2 Å)/AFt composite. However, it just shows how deformation was applied. To calculate the elastic constants, it only requires a small deformation. A strain of 1%, at this scale, seems to be a good compromise between an accurate determination of the slope in the stress-strain curve and an acceptable calculation time. We used strain rate of 10^{-6}/fs or 10^{-5}/fs for all simulations in this paper. The study of sensitivity on the strain rate was carried out with direct tension test simulations. This study made us retain the strain rate of 10^{-6}/fs and 10^{-5}/fs for the calculation of elastic constants. This choice was made on the one hand by determining the velocity from which the results in term of stress-strain curve no longer evolved, and on the other hand by checking the stability conditions for VRH approximation. The results of elastic constants were likewise obtained from the initial linear part of the obtained stress-strain curves by $C_{ij} = \partial\sigma_i/\partial\varepsilon_j$ (i,j = 1,2,3,4,5,6) where $\varepsilon_1 = \varepsilon_{xx}$, $\varepsilon_2 = \varepsilon_{yy}$, $\varepsilon_3 = \varepsilon_{zz}$, $\varepsilon_4 = \varepsilon_{yz}$, $\varepsilon_5 = \varepsilon_{xz}$ and $\varepsilon_6 = \varepsilon_{xy}$. Finally, the elastic constants values were averaged along the symmetric matrix.

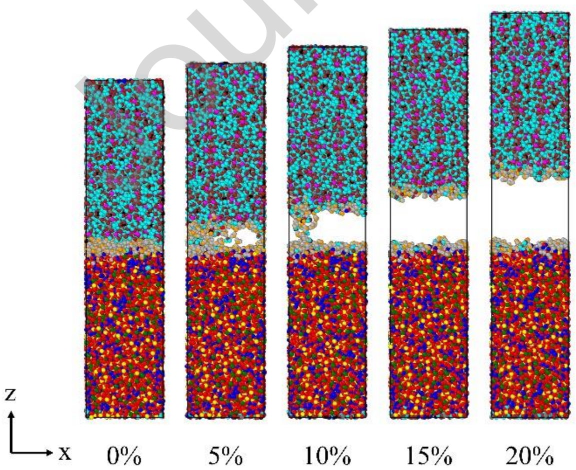

Fig. 6. Direct tension test in z-direction in xz plan from the state after NPT relaxation to 20% strain with C-S-H (I)/H_2O (6.2 Å)/AFt composite.

With elastic constants, it is possible to calculate Young's modulus (E_{VRH}) and Poisson's ratio (ν_{VRH}) via Voigt-Reuss-Hill (VRH) approximation scheme. It should be noted that calculations are not the same for different space groups.

For monoclinic space group (i.e., C-S-H (I)), calculations of shear moduli and bulk moduli of Reuss and Voigt bounds are as the following [37]:

$$G_V = \frac{1}{15}[C_{11} + C_{22} + C_{33} + 3(C_{44} + C_{55} + C_{66}) - (C_{12} + C_{13} + C_{23})] \tag{2}$$

$$\begin{aligned} G_R = 15\{&4[(C_{33}C_{55} - C_{35}^2)(C_{11} + C_{22} + C_{12}) + (C_{23}C_{55} \\ &- C_{25}C_{35})(C_{11} - C_{12} - C_{23}) + (C_{13}C_{35} - C_{15}C_{33})(C_{15} + C_{25}) \\ &+ (C_{13}C_{55} - C_{15}C_{35})(C_{22} - C_{12} - C_{23} - C_{13}) \\ &+ (C_{13}C_{25} - C_{15}C_{23})(C_{15} - C_{25}) + C_{77}/\Omega \\ &+ 3[C_{77}/\Omega + (C_{44} + C_{66})/(C_{44}C_{66} - C_{46}^2)]\}^{-1} \end{aligned} \tag{3}$$

$$K_V = [C_{11} + C_{22} + C_{33} + 2(C_{12} + C_{13} + C_{23})] / 9 \tag{4}$$

$$\begin{aligned} K_R = \Omega[&(C_{33}C_{55} - C_{35}^2)(C_{11} + C_{22} - 2C_{12}) \\ &+ (C_{23}C_{55} - C_{25}C_{35})(2C_{12} - 2C_{11} - C_{23}) \\ &+ (C_{13}C_{55} - C_{15}C_{33})(C_{15} - 2C_{25}) \\ &+ (C_{13}C_{55} - C_{15}C_{35})(2C_{12} + 2C_{23} - C_{13} - 2C_{22}) \\ &+ 2(C_{13}C_{25} - C_{15}C_{23})(C_{25} - C_{15}) + C_{77}]^{-1} \end{aligned} \tag{5}$$

$$\Delta = \Delta_{11}(\Delta_{22}\Delta_{55} - \Delta_{25}^2) - \Delta_{12}(\Delta_{12}\Delta_{55} - \Delta_{15}\Delta_{25}) + \Delta_{15}(\Delta_{12}\Delta_{25} - \Delta_{15}\Delta_{22}) + \Delta_{25}(\Delta_{23}\Delta_{35} - \Delta_{25}\Delta_{33}) \quad (6)$$

$$\Delta_1 = \Delta_{11}\Delta_{22}\Delta_{33} - \Delta_{11}\Delta_{23}^2 - \Delta_{22}\Delta_{13}^2 - \Delta_{33}\Delta_{12}^2 + 2\Delta_{12}\Delta_{13}\Delta_{23} \quad (7)$$

$$\Delta_2 = 2[\Delta_{15}\Delta_{25}(\Delta_{33}\Delta_{12} - \Delta_{13}\Delta_{23}) + \Delta_{15}\Delta_{35}(\Delta_{22}\Delta_{13} - \Delta_{12}\Delta_{23}) + \Delta_{25}\Delta_{35}(\Delta_{11}\Delta_{23} - \Delta_{12}\Delta_{13})] - [\Delta_{15}^2(\Delta_{22}\Delta_{33} - \Delta_{23}^2) + \Delta_{25}^2(\Delta_{11}\Delta_{33} - \Delta_{13}^2) + \Delta_{35}^2(\Delta_{11}\Delta_{22} - \Delta_{12}^2)] + \Delta_1\Delta_{55} \quad (8)$$

The VRH estimation of the two moduli correspond to the arithmetic mean values:

$$B_H = (B_R + B_V)/2 \quad (9)$$

$$G_H = (G_R + G_V)/2 \quad (10)$$

The Young's modulus and Poisson's ratio can now be estimated:

$$E = 9BG/(3B + G) \quad (11)$$

$$\nu = (3B - 2G)/2(3B + G) \quad (12)$$

There are seven mechanical stability conditions to respect for monoclinic space group [37]:

$$\Delta_{sous} > 0, (i = 1,2,3,4,5,6) \quad (13)$$

$$(C_{44}C_{66} - C_{46}^2) > 0 \tag{14}$$

$$(C_{33}C_{55} - C_{35}^2) > 0 \tag{15}$$

$$(C_{22} + C_{33} - 2C_{23}) > 0 \tag{16}$$

$$[C_{11} + C_{22} + C_{33} + 2(C_{12} + C_{13} + C_{23})] > 0 \tag{17}$$

$$[C_{22}(C_{33}C_{55} - C_{35}^2) + 2C_{23}C_{25}C_{35} - C_{23}^2C_{55} - C_{25}^2C_{33}] > 0 \tag{18}$$

$$\begin{aligned}\{2[C_{15}C_{25}(C_{33}C_{12} - C_{13}C_{23}) + C_{15}C_{35}(C_{22}C_{13} - C_{12}C_{23}) \\ + C_{25}C_{35}(C_{11}C_{23} - C_{12}C_{13})] - [C_{15}^2(C_{22}C_{33} - C_{23}^2) \\ + C_{25}^2(C_{11}C_{33} - C_{13}^2) + C_{35}^2(C_{11}C_{22} - C_{12}^2)] + C_{11}C_{55}\} > 0\end{aligned} \tag{19}$$

For trigonal space group (i.e., CH and AFt), calculations of shear and bulk moduli of Voigt and Reuss bounds are as the following [38]:

$$G_{Voigt} = \frac{(C_{11} + C_{22} + C_{33}) - (C_{12} + C_{23} + C_{31}) + 3(C_{44} + C_{55} + C_{66})}{15} \tag{20}$$

$$G_{Reuss} = \frac{15}{4(S_{11} + S_{22} + S_{33}) - 4(S_{12} + S_{23} + S_{31}) + 3(S_{44} + S_{55} + S_{66})} \tag{21}$$

$$B_{Voigt} = \frac{C_{11} + C_{22} + C_{33} + 2(C_{12} + C_{23} + C_{31})}{9} \tag{22}$$

$$B_V = \frac{1}{C_{11} + C_{22} + C_{33} + 2(C_{12} + C_{23} + C_{31})} \tag{23}$$

$$C_{11} = \frac{B_1 B_3 B_{44} - B_3 B_4^2 - B_{44} B_{13}^2}{B_3 B_{44} B_{11} - 2B_{11} B_{13} B_{14} - B_3 B_{44} B_{12} - 2B_{12} B_3 B_{14} - 2B_{11} B_{44} B_{13} + 2B_{12} B_{44} B_{13} + 4B_{13}^2 B_{14}} \tag{24}$$

$$C_{12} = -\frac{B_2 B_3 B_{44} + B_3 B_{14}^2 - B_{44} B_{13}^2}{B_3 B_{44} B_{11} - 2B_{11} B_{13} B_{14} - B_3 B_{44} B_{12} - 2B_{12} B_3 B_{14} - 2B_{11} B_{44} B_{13} + 2B_{12} B_{44} B_{13} + 4B_{13}^2 B_{14}} \tag{25}$$

$$C_{13} = -\frac{B_{13}}{B_{11} B_3 + B_{12} B_3 - 2B_{13}^2} \tag{26}$$

$$C_{14} = -\frac{B_{14}}{B_{11} B_{44} - B_{12} B_{44} - 2B_{14}^2} \tag{27}$$

$$C_{23} = \frac{B_{11} + B_{12}}{B_{11} B_3 + B_{12} B_3 - 2B_{13}^2} \tag{28}$$

$$C_{24} = \frac{B_{11} - B_{12}}{B_{11} B_{44} - B_{12} B_{44} - 2B_{14}^2} \tag{29}$$

$$C_{66} = 2(C_{11} - C_{12}) \tag{30}$$

The results should be respected by these three following mechanical stability conditions [38]:

$$B_{11} > |B_{12}| \tag{31}$$

$$(k_{11} + k_{12})k_{33} - 2k_{13}^2 > 0 \tag{32}$$

$$(k_{11} - k_{12})k_{44} - 2k_{14}^2 > 0 \tag{33}$$

2.4.5. Homogenization scheme

The study was started from the phase composition of hardened cement paste (HCP) with w/c ratio of 0.4. The cement paste was supposed to be well hydrated and consequently few unhydrated phases should be present. Then a simplified hardened cement paste without unhydrated phases was considered. We suppose C-S-H (I) phase or gel represented by C-S-H (I) of 53%, CH phase of 19%, sulfoaluminate phase represented by AFt of 10% and capillary porosity of 18% [39]. It should be noticed that C-S-H phase includes low density C-S-H (I) about 70% and high density C-S-H (II) about 30% with the nanoporosity of 35% and 24%, respectively [40].

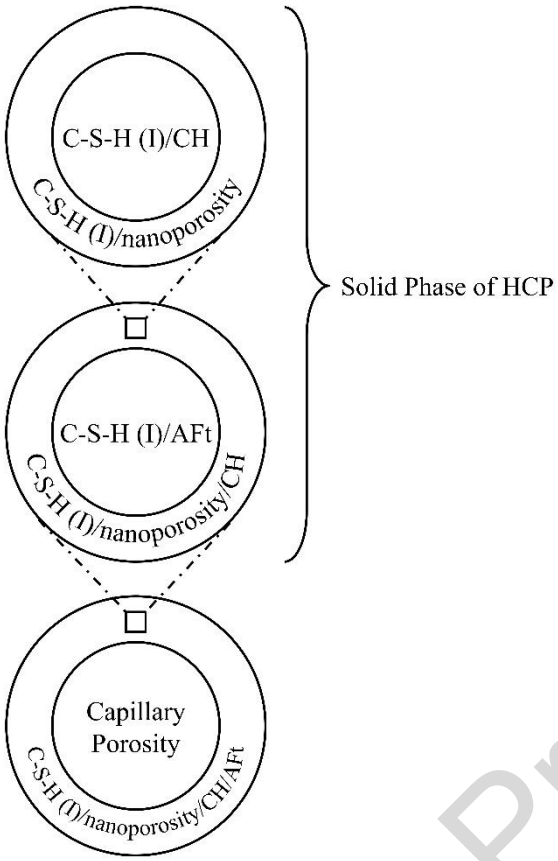

Fig. 7. Scheme of homogenization procedure of simplified hardened cement paste.

Fig. 7 shows step-by-step the homogenization procedure in order to obtain the homogenization of simplified HCP. Fu et al. [6] did the determination of elastic modulus assessment of LD and HD C-S-H using self-consistent and Mori-Tanaka schemes. In their study, self-consistent scheme could only be used to calculate Young's modulus up to 50% of porosity volume fraction. On the other hand, Mori-Tanaka scheme could be used to calculate the elastic modulus up to 100% of porosity volume fraction. Since porosity volume fraction of C-S-H (I)/nanoporosity is 70%, Mori-Tanka scheme is one of the choice to be used to calculate Young's modulus and Poisson's ratio in our study. First, Mori-Tanaka homogenization scheme was used between C-S-H (I), considered as the matrix, and nanoporosity, considered as the inclusion. Then,

homogenization scheme between C-S-H (I)/nanoporosity and C-S-H (I)/CH gave results of C-S-H (I)/nanoporosity/CH matrix. Next, homogenization scheme was performed between C-S-H (I)/nanoporosity/CH matrix and C-S-H (I)/AFt. Finally, the homogenization scheme was applied between capillary porosity and solid phase, which is the matrix of C-S-H (I)/nanoporosity/CH/AFt, to obtain a simplified HCP.

With Mori-Tanaka scheme, shear and bulk moduli of the homogenous matrix is calculated following these expressions [32]:

$$k_{hom} = \frac{\sum_r f_r k_r \left(1 + \alpha_s\left(\frac{k_r}{k_s} - 1\right)\right)^{-1}}{\sum_r f_r \left(1 + \alpha_s\left(\frac{k_r}{k_s} - 1\right)\right)^{-1}} \tag{34}$$

$$g_{hom} = \frac{\sum_r f_r g_r \left(1 + \beta_s\left(\frac{g_r}{g_s} - 1\right)\right)^{-1}}{\sum_r f_r \left(1 + \beta_s\left(\frac{g_r}{g_s} - 1\right)\right)^{-1}} \tag{35}$$

Where f_r is the volume fraction of the first phase (the matrix), the coefficients α_s and β_s are given by:

$$\alpha_s = \frac{3k_s}{3k_s + 4g_s} \tag{36}$$

$$\beta_s = \frac{6(k_s + 2g_s)}{5(3k_s + 4g_s)} \tag{37}$$

In all these expressions, g_r and g_s are the shear moduli of the matrix and the inclusion respectively; k_r and k_s are the bulk moduli:

$$G_{water} = \frac{E_{water}}{2(1 + \nu_{water})]} \tag{38}$$

$$K_{water} = \frac{E_{water}}{3(1 - 2\nu_{water})} \tag{39}$$

The bulk and shear moduli of water are 0 and 2.2 GPa, respectively. Poisson's ratio of water was taken equal to 0.5.

3. Results and Discussion

3.1. Elastic constants, Young's moduli and Poisson's ratios

3.1.1. Calcium-Silicate-Hydrate (C-S-H (I))

Table 1 shows elastic constants of C-S-H (I)/C-S-H (I) composite with monoclinic space group following procedure on **section 2.4.2**. Thirteen elastic constants values were calculated for orientation in y- and in z-directions. Elastic constants of counterclockwise rotated in y-direction could be found in **Table 2**. Young's moduli and Poisson's ratios of this composite are shown in **Fig. 8**.

Table 1 Elastic constants (in GPa) of C-S-H (I)/C-S-H (I) in y- and z-directions.

	y-direction			z-direction		
Spacing	1 Å vacuum	3.1 Å water	6.2 Å water	1 Å vacuum	3.1 Å water	6.2 Å water
C_{11}	71.901	59.886	68.431	78.572	72.109	70.941
C_{22}	82.925	55.623	45.792	83.128	80.611	71.606
C_{33}	76.332	62.131	67.986	70.973	65.629	24.678
C_{44}	20.879	14.017	11.840	20.713	17.547	11.645

C_{55}	19.199	17.649	18.826	19.431	15.062	5.610
C_{66}	20.803	11.394	7.621	19.574	21.906	18.900
C_{12}	36.312	28.337	15.318	45.666	38.612	35.648
C_{13}	32.353	28.920	31.675	39.022	36.099	14.001
C_{15}	4.482	1.543	4.988	0.435	-0.005	1.891
C_{23}	37.363	27.846	14.659	40.491	36.736	16.606
C_{25}	-1.373	2.539	-1.685	2.387	-0.049	2.665
C_{35}	-2.414	-1.078	1.925	0.865	0.590	-2.306
C_{46}	1.203	-0.548	-2.477	-0.018	4.419	-0.403

Table 2 Elastic constants (in GPa) of C-S-H (I)/C-S-H (I) counterclockwise rotated in y-direction.

Spacing	1 Å vacuum	3.1 Å water	6.2 Å water
C_{11}	74.594	69.468	61.278
C_{22}	73.288	61.975	34.722
C_{33}	70.713	67.075	63.017
C_{44}	17.699	13.210	3.851
C_{55}	21.756	16.553	16.214
C_{66}	19.181	13.763	1.238
C_{12}	39.316	33.897	18.148
C_{13}	33.258	33.431	30.674
C_{15}	1.004	-1.313	3.548
C_{23}	37.567	33.595	18.129
C_{25}	-0.936	0.939	2.252
C_{35}	-2.219	0.648	1.329
C_{46}	0.381	0.478	0.313

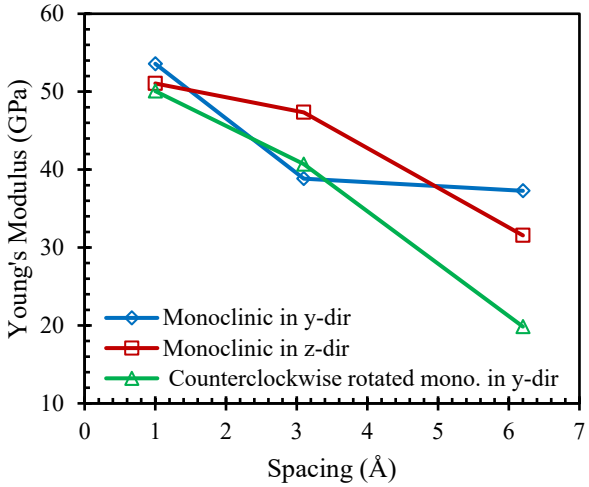

(a)

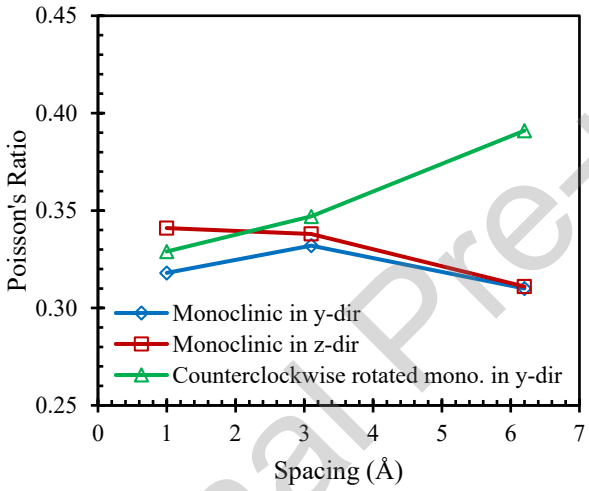

(b)

Fig. 8. Curves of (a) Young's modulus, (b) Poisson's ratio and spacing between supercells with three different orientations of C-S-H (I)/C-S-H (I) composite.

3.1.2. Calcium-Silicate-Hydrate/Portlandite (C-S-H (I)/CH)

For C-S-H (I)/CH composite, calculation of elastic constants was also followed by **section 2.4.2**. However, sixteen elastic constants values were calculated as a result of combination of monoclinic and trigonal space group. **Table 3** shows the results in y-, and in z-directions with different spacing of vacuum and water between C-S-H (I)/CH composite. In addition, **Table 4** shows results of elastic constants of C-S-H (I)/CH composite where supercell CH was counterclockwise rotated around x-axis in y-

direction on the side of supercell C-S-H (I). Young's moduli and Poisson's ratios of C-S-H (I)/CH composite were calculated by both monoclinic space group and trigonal space group as shown in **Fig. 9** because C-S-H (I) has a monoclinic space group, and CH has a trigonal space group.

Table 3 Elastic constants (in GPa) of C-S-H (I)/CH in y- and z-directions.

	y-direction			z-direction		
Spacing	1 Å vacuum	3.1 Å water	6.2 Å water	1 Å vacuum	3.1 Å water	6.2 Å water
C_{11}	85.478	71.444	74.429	72.715	71.487	71.757
C_{22}	76.749	69.482	57.284	72.065	74.978	63.519
C_{33}	50.927	48.038	52.582	42.504	37.467	24.904
C_{44}	9.789	9.849	5.306	7.013	7.643	4.968
C_{55}	15.288	11.974	12.634	9.536	7.796	2.256
C_{66}	21.235	18.897	7.213	19.962	18.102	15.614
C_{12}	36.896	29.573	28.319	31.811	43.123	36.276
C_{13}	28.497	26.756	26.773	22.697	24.214	18.247
C_{15}	-0.121	-0.127	0.437	-1.519	4.462	2.244
C_{23}	30.976	28.393	24.736	22.155	18.797	16.015
C_{25}	2.038	1.551	4.738	0.658	1.798	-3.494
C_{35}	-0.147	-0.415	3.913	0.192	0.596	-1.789
C_{46}	-1.194	1.937	-2.556	1.434	-0.288	0.108
C_{14}	-0.238	-0.589	-5.967	-9.401	-6.978	-3.497
C_{24}	11.598	5.441	3.178	2.584	7.740	4.644
C_{56}	-2.302	-2.752	-2.723	-6.071	-8.642	-4.369

Table 4 Elastic constants (in GPa) of C-S-H (I)/CH counterclockwise rotated in y-direction.

Spacing	1 Å vacuum	3.1 Å water	6.2 Å water

C_{11}	79.728	72.632	71.067
C_{22}	37.185	42.516	34.190
C_{33}	67.853	70.340	69.348
C_{44}	7.101	7.309	4.285
C_{55}	18.746	19.400	19.964
C_{66}	6.297	7.612	7.473
C_{12}	20.380	19.514	19.948
C_{13}	43.107	38.052	36.410
C_{15}	0.461	0.02655	0.398
C_{23}	21.412	20.606	19.429
C_{25}	0.589	2.40825	-0.061
C_{35}	-1.047	0.1774	-3.117
C_{46}	0.282	-1.1184	0.841
C_{14}	8.781	3.030	7.921
C_{24}	2.828	-2.659	3.477
C_{56}	6.545	2.918	5.696

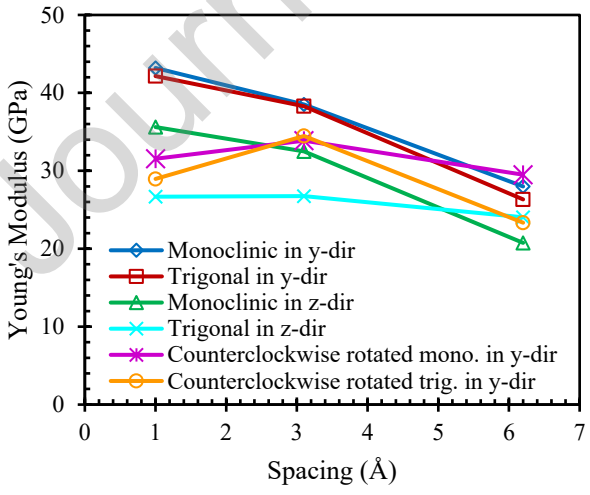

(a)

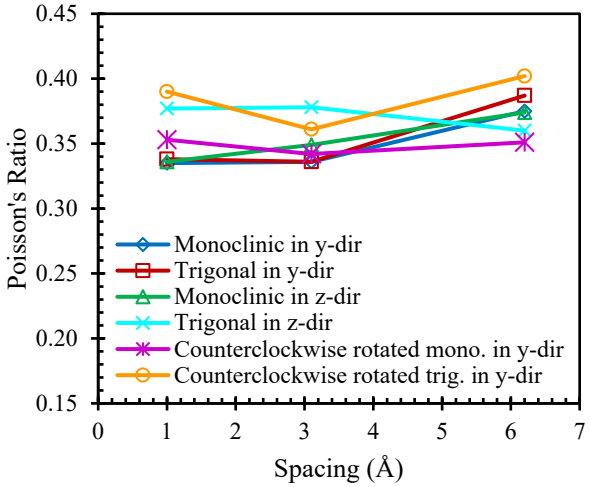

(b)

Fig. 9. Curves of (a) Young's modulus, (b) Poisson's ratio and spacing between supercells with three different orientations of C-S-H (I)/CH composite.

3.1.3. Calcium-Silicate-Hydrate/Ettringite (C-S-H (I)/AFt)

Similarly, elastic constants of C-S-H (I)/AFt composite were also calculated following **section 2.4.2**. Young's moduli were calculated by both monoclinic and trigonal space group since AFt has also a trigonal space group. **Table 5** shows the results of elastic constants in y- and z-directions. Additionally, **Table 6** shows the results of elastic constants of C-S-H (I)/AFt composite where AFt supercell was counterclockwise rotated in y-direction. The results of Young's moduli and Poisson's ratios of this composite could be found in **Fig. 10**.

Table 5 Elastic constants (in GPa) of C-S-H (I)/AFt in y- and z-directions.

	y-direction			z-direction		
Spacing	1 Å vacuum	3.1 Å water	6.2 Å water	1 Å vacuum	3.1 Å water	6.2 Å water
C_{11}	39.426	37.727	34.862	44.836	45.037	43.244
C_{22}	25.101	28.133	14.241	50.547	42.344	41.653

C_{33}	50.688	46.793	42.433	48.823	35.221	24.367
C_{44}	4.625	2.768	7.209	10.000	5.276	2.115
C_{55}	14.046	10.042	8.365	8.100	1.891	2.486
C_{66}	4.896	5.066	6.594	10.603	11.797	12.594
C_{12}	13.719	13.449	4.478	22.978	23.738	20.446
C_{13}	20.018	16.465	13.519	19.202	19.354	12.199
C_{15}	2.151	3.520	-7.303	0.139	-1.466	2.841
C_{23}	15.874	13.779	5.452	23.317	17.567	11.069
C_{25}	-0.178	-0.358	-6.565	1.037	0.350	-1.904
C_{35}	1.954	1.641	-5.288	3.152	-1.491	-2.217
C_{46}	0.799	0.016	-2.110	1.236	-0.144	-0.013
C_{14}	-3.277	3.603	-4.342	2.015	2.601	-0.281
C_{24}	-2.369	-1.258	-1.789	4.345	-1.058	2.758
C_{56}	1.608	0.826	-2.456	-0.161	-0.169	-1.606

Table 6 Elastic constants (in GPa) of C-S-H (I)/AFt counterclockwise rotated in y-direction.

Spacing	1 Å vacuum	3.1 Å water	6.2 Å water
C_{11}	40.568	33.405	39.456
C_{22}	47.721	38.035	38.366
C_{33}	42.072	36.884	41.433
C_{44}	7.886	6.828	8.323
C_{55}	9.329	9.397	8.796
C_{66}	8.051	3.798	4.660
C_{12}	19.711	17.007	16.734
C_{13}	22.346	20.489	18.881
C_{15}	0.954	0.163	-0.091
C_{23}	18.876	16.715	14.072
C_{25}	-0.935	0.690	1.657
C_{35}	0.527	-1.721	0.325

C_{46}	-1.221	-0.707	0.840
C_{14}	1.887	-1.085	-1.105
C_{24}	0.809	0.386	-2.504
C_{56}	-0.711	-0.723	0.067

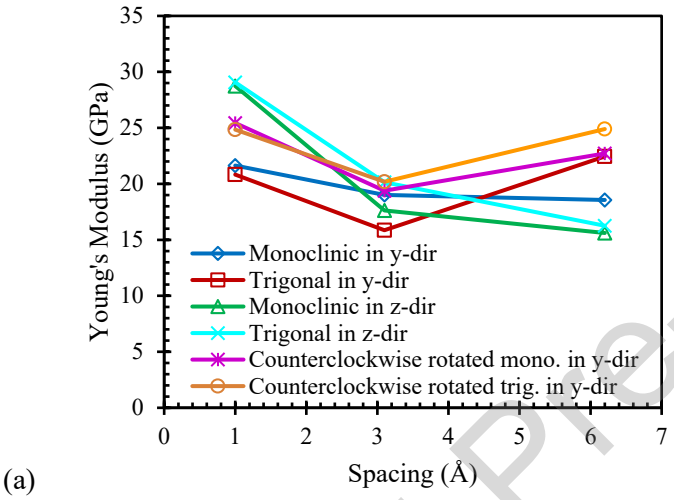

(a)

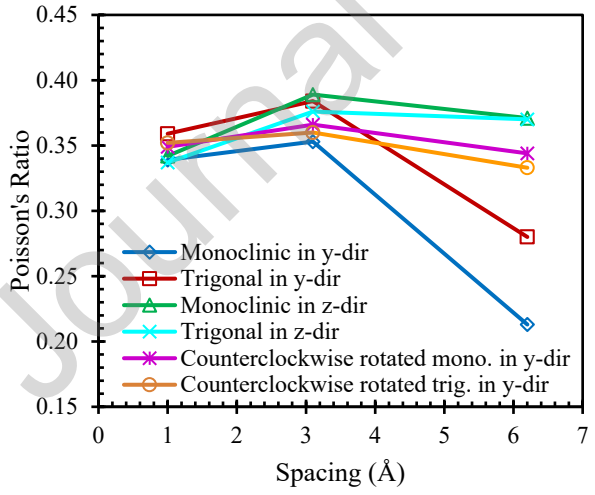

(b)

Fig. 10. Curves of (a) Young's modulus, (b) Poisson's ratio and spacing between supercells with three different orientations of C-S-H (I)/AFt composite.

3.1.4. Homogenization of simplified HCP

In order to calculate the homogenization of simplified HCP, the values of Young's modulus and Poisson's ratio were averaged among the three orientations: in y-, in z-, and counterclockwise rotated in y-directions. **Table 7** shows these mean values.

Table 7 Mean Young's modulus (in GPa) and Poisson's ratio of three orientations.

Composite	Space group	Spacing	E (GPa)	υ
C-S-H (I)/C-S-H (I)	Monoclinic	1 Å vacuum	51.569	0.329
		3.1 Å water	42.296	0.339
		6.2 Å water	29.559	0.337
C-S-H (I)/CH	Monoclinic	1 Å vacuum	36.786	0.341
		3.1 Å water	34.960	0.342
		6.2 Å water	26.081	0.367
	Trigonal	1 Å vacuum	32.598	0.368
		3.1 Å water	33.169	0.358
		6.2 Å water	24.568	0.383
C-S-H (I)/AFt	Monoclinic	1 Å vacuum	25.271	0.343
		3.1 Å water	18.676	0.369
		6.2 Å water	18.964	0.309
	Trigonal	1 Å vacuum	24.915	0.349
		3.1 Å water	18.730	0.373
		6.2 Å water	21.199	0.328

Following scheme on **Fig. 7** and **Eq. (34) - (39)**, Young's moduli and Poisson's ratios of homogenization of simplified HCP were obtained (see **Fig. 11)**.

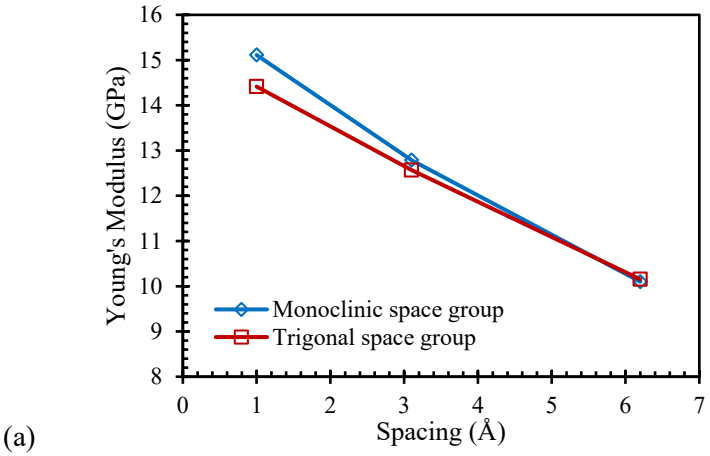

(a)

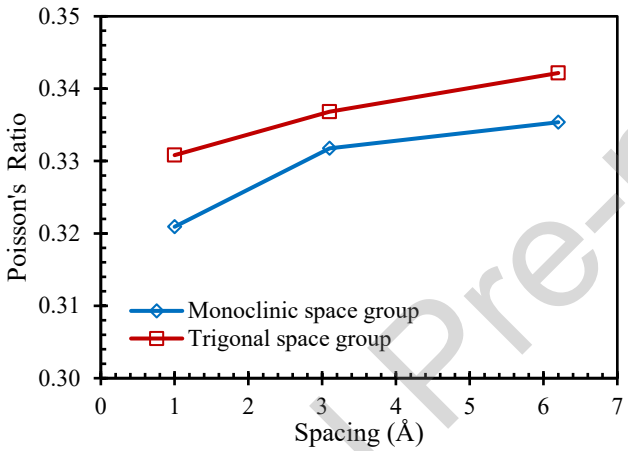

(b)

Fig. 11. Curves of (a) Young's modulus, and (b) Poisson's ratio with different spacing of two different space groups using Mori-Tanaka scheme with simplified HCP.

3.2. Discussion

In this paper, all Reactive Molecular Dynamics simulations to obtain elastic constants values were done with strain rates of 10^{-6}/fs or 10^{-5}/fs. With the values of elastic constants, VRH approximation makes it possible to obtain Young's modulus and Poisson's ratio of main hydrated cement paste phases composites. Young's modulus and Poisson's ratio of C-S-H (I)/C-S-H (I) composite with 1 Å vacuum spacing were found to be 51.6 GPa and 0.329, respectively. When the spacing increases up to 3.1 Å and 6.2 Å, with water molecules in between the two phases, the Young's modulus

decreased and was equal to 42.3 GPa and 29.6 GPa, respectively. The value of 42.3 GPa might be compared to the result obtained by Bonnaud et al. [34] (mean value of 40.1 GPa) for a similar spacing. Both results are in good agreement. And thus, even if the force fields between atoms are different and the procedure is totally different as Bonnaud et al. evaluated the mean forces and interaction Grand Potential between C-S-H nanoparticles through Grand canonical Monte Carlo simulations.

To the authors' knowledge, simulations of C-S-H (I)/CH composite were only done by Liang [33]. In their study, they placed CH phase about 3 Å on top of C-S-H phase. They found the Young's modulus to be about 40 GPa. Compared to their results, C-S-H (I)/CH composite results with 1 Å vacuum spacing with trigonal and monoclinic space group were 32.6 GPa and 36.8 GPa, respectively. The result of monoclinic space group seems to be much closer to the result obtained by Liang than the one with trigonal space group. The methods to obtain Young's modulus are different. They calculated the values of Young's modulus from stress-strain curve of uniaxial tensile test. In our study, VRH approximation was used. As could be seen, different orientations in y-, in z-, and counterclockwise in y-directions gave different values of Young's modulus and Poisson's ratio. Space group and spacing of vacuum and water also led to quite different results.

For the first time, the Young's modulus and the Poisson's ratio of C-S-H/AFt composites have been calculated. Considering a monoclinic space group, the Young's modulus of this composite decreased from 25.3 to 19 GPa when the interlayer spacing grew up from 1 Å to 6.2 Å. The Poisson's ratio also decreased, from 0.343 to 0.309. In the same time, considering a trigonal space group, the Young's modulus presented a

minimal value of 18.7 GPa for a spacing of 3.1 Å. The Poisson's ratio still decreases from 0.349 to 0.328. No literature value has been found for a sake of comparison. All these values of Young's moduli and Poisson's ratios were averaged among three orientations. For spacing between supercells approximately equaled to the one determined by Bonnaud et al. [34] for C-S-H globules, the Young's modulus of C-S-H (I)/C-S-H (I), C-S-H (I)/CH and C-S-H (I)/AFt were respectively equal to 42.3 GPa, 34.1 GPa and 18.7 GPa. Note that, for the two last ones, mean values between trigonal and monoclinic space groups have been provided. These results also enabled the calculation of homogenization of simplified HCP via Mori-Tanaka scheme as shown in **Fig. 11a**. The results ranged from 10.100 GPa to 15.112 GPa and from 0.321 to 0.342 for Young's modulus and Poisson's ratio, respectively. It should be noticed that results in this paper were obtained from a simplified hardened cement paste without taking into account unhydrated phases and including only three main hydrated cement phases (i.e., AFt, CH and C-S-H (I)). As a result, it is not easy to compare with results of normal hardened cement paste. Especially, taking into account unhydrated phases might increase the values of Young's modulus since their Young's modulus are very high.

4. Conclusion and future work

In this paper, elastic constants of composite hydrated cement paste phases were calculated using the molecular dynamics software called LAMMPS. The effort was focused here on the adhesion between the different phases of the hydrated cement paste. Supercells of C-S-H (I), CH and Aft have been constructed. The adhesion between the supercells was taken into account by means of Reactive Molecular Dynamics simulations. Various configurations of spacing were considered too: 1 Å vacuum, 3.1 Å

water and 6.2 Å water spacing. The combination of two phases of cement paste was called cement paste composite in this study. Thus C-S-H (I)/C-S-H (I), C-S-H (I)/CH and C-S-H (I)/Aft composites were considered. Their Elastic Constants were calculated from the slope of stress-strain curves with 1% strain in six different deformations of composite supercells.

The elastic constants could be used to calculate homogenized Young's modulus and Poisson's ratio via Voigt-Reuss-Hill approximation. Two different methods were used to calculate Young's modulus and Poisson's ratio depending on space group (i.e., monoclinic and trigonal space groups). For the mean value of spacing (3.1 Å) the Young's modulus of C-S-H (I)/C-S-H (I), C-S-H (I)/CH and C-S-H (I)/AFt were found to be respectively equal to 42.3 GPa, 34.1 GPa and 18.7 GPa.

Moreover, with these results, it was also possible to obtain Young's modulus and Poisson's ratio of simplified hardened cement paste with homogenization scheme (i.e., Mori-Tanaka scheme). Results were found in range between 10.1 GPa and 15.1 GPa, and between 0.32 and 0.34 for Young's modulus and Poisson's ratio, respectively. It should be noted that these values were calculated from simplified hardened cement paste without taking into account the unhydrated phases. It might be possible to use this method to obtain normal hardened cement paste by calculating elastic constants of different composites with other hydrated and unhydrated phases. This paper might contribute to make it possible the bridge of achieving transition from molecular scale to continuous microscopic scale.

On the condition of paying attention to the simulation and calculation procedures as well as to the formulas of VRH approximation, which must all be adapted to the crystallographic groups, this work could be continued in order to take into account other

secondary phases of the cementitious matrices (anhydrous phases, gypsum, different forms of hydrated calcium aluminates...) and to obtain a more precise estimate of the mechanical properties of hydrated cement pastes. This work could also be extended to other heterogeneous materials, such as reinforced composites on which the scientific literature is abundant (for instance [42-45]).

References

[1] D. Keinde, S. Kamali-Bernard, F. Bernard, I. Cisse, Effect of the interfacial transition zone and the nature of the matrix-aggregate interface on the overall elastic and inelastic behaviour of concrete under compression: a 3D numerical study, Eur. J. Environ. Civ. Eng. 18 (2014) 1167–1176. https://doi.org/10.1080/19648189.2014.896757.

[2] D. Lau, W. Jian, Z. Yu, D. Hui, Nano-engineering of construction materials using molecular dynamics simulations: Prospects and challenges, Compos. Part B Eng. 143 (2018) 282–291. https://doi.org/10.1016/j.compositesb.2018.01.014.

[3] K. Ioannidou, Mesoscale Structure and Mechanics of C-S-H, in: W. Andreoni, S. Yip (Eds.), Handb. Mater. Model. Appl. Curr. Emerg. Mater., Springer International Publishing, Cham, 2020: pp. 1–15. https://doi.org/10.1007/978-3-319-50257-1_127-1.

[4] H.F.W. Taylor, Cement chemistry, 2. ed., Repr, Telford, London, 1997.

[5] A.E. Moore, H.F.W. Taylor, Crystal structure of ettringite, Acta Crystallogr. B. 26 (1970) 386–393. https://doi.org/10.1107/S0567740870002443.

[6] J. Fu, S. Kamali-Bernard, F. Bernard, M. Cornen, Comparison of mechanical properties of C-S-H and portlandite between nano-indentation experiments and a modeling approach using various simulation techniques, Compos. Part B Eng. 151 (2018) 127–138. https://doi.org/10.1016/j.compositesb.2018.05.043.

[7] F. Bernard, S. Kamali-Bernard, W. Prince, 3D multi-scale modelling of mechanical behaviour of sound and leached mortar, Cem. Concr. Res. 38 (2008) 449–458. https://doi.org/10.1016/j.cemconres.2007.11.015.

[8] J. Claverie, S. Kamali-Bernard, J.M.M. Cordeiro, F. Bernard, Assessment of mechanical, thermal properties and crystal shapes of monoclinic tricalcium silicate from atomistic simulations, Cem. Concr. Res. 140 (2021) 106269. https://doi.org/10.1016/j.cemconres.2020.106269.

[9] X. Gao, Y. Wei, W. Huang, Effect of individual phases on multiscale modeling mechanical properties of hardened cement paste, Constr. Build. Mater. 153 (2017) 25–35. https://doi.org/10.1016/j.conbuildmat.2017.07.074.

[10] S. Kamali-Bernard, F. Bernard, Effect of tensile cracking on diffusivity of mortar: 3D numerical modelling, Comput. Mater. Sci. 47 (2009) 178–185. https://doi.org/10.1016/j.commatsci.2009.07.005.

[11] A. Rhardane, S. Al Haj Sleiman, S.Y. Alam, F. Grondin, A quantitative assessment of the parameters involved in the freeze–thaw damage of cement-based materials through numerical modelling, Constr. Build. Mater. 272 (2021) 121838. https://doi.org/10.1016/j.conbuildmat.2020.121838.

[12] A. Rhardane, F. Grondin, S.Y. Alam, Development of a micro-mechanical model for the determination of damage properties of cement pastes, Constr. Build. Mater. 261 (2020) 120514. https://doi.org/10.1016/j.conbuildmat.2020.120514.

[13] T. Honorio, P. Guerra, A. Bourdot, Molecular simulation of the structure and elastic properties of ettringite and monosulfoaluminate, Cem. Concr. Res. 135 (2020) 106126. https://doi.org/10.1016/j.cemconres.2020.106126.

[14] T. Honorio, Monte Carlo Molecular Modeling of Temperature and Pressure Effects on the Interactions between Crystalline Calcium Silicate Hydrate Layers, Langmuir. (2019). https://doi.org/10.1021/acs.langmuir.8b04156.

[15] E. Del Gado, K. Ioannidou, E. Masoero, A. Baronnet, R.J.-M. Pellenq, F.-J. Ulm, S. Yip, A soft matter in construction – Statistical physics approach to formation

and mechanics of C–S–H gels in cement, Eur. Phys. J. Spec. Top. 223 (2014) 2285–2295. https://doi.org/10.1140/epjst/e2014-02264-1.

[16] Y. Zhou, D. Hou, H. Manzano, C.A. Orozco, G. Geng, P.J.M. Monteiro, J. Liu, Interfacial Connection Mechanisms in Calcium–Silicate–Hydrates/Polymer Nanocomposites: A Molecular Dynamics Study, ACS Appl. Mater. Interfaces. 9 (2017) 41014–41025. https://doi.org/10.1021/acsami.7b12795.

[17] H. Manzano, J.S. Dolado, A. Ayuela, Elastic properties of the main species present in Portland cement pastes, Acta Mater. 57 (2009) 1666–1674. https://doi.org/10.1016/j.actamat.2008.12.007.

[18] H. Manzano, E. Masoero, I. Lopez-Arbeloa, H.M. Jennings, Shear deformations in calcium silicate hydrates, Soft Matter. 9 (2013) 7333–7341. https://doi.org/10.1039/C3SM50442E.

[19] P.C. Hewlett, Lea's Chemistry of Concrete and Cement, Elsevier, Oxford, 1998.

[20] L. Desgranges, D. Grebille, G. Calvarin, G. Chevrier, N. Floquet, J.-C. Niepce, Hydrogen thermal motion in calcium hydroxide: Ca(OH)2, Acta Crystallogr. B. 49 (1993) 812–817. https://doi.org/10.1107/S0108768193003556.

[21] F. Goetz-Neunhoeffer, J. Neubauer, Refined ettringite (Ca6Al2(SO4)3(OH)12·26H2O) structure for quantitative X-ray diffraction analysis, Powder Diffr. 21 (2006) 4–11. https://doi.org/10.1154/1.2146207.

[22] S.A. Hamid, The crystal structure of the 11Å natural tobermorite Ca2.25[Si3O7.5(OH)1.5] · 1H2O, Z. Für Krist. - Cryst. Mater. 154 (1981) 189–198. https://doi.org/10.1524/zkri.1981.154.3-4.189.

[23] J. Fu, Multiscale modeling and mechanical properties of typical anisotropic crystals structures at nanoscale, INSA Rennes, 2016. https://www.theses.fr/s121120.

[24] D. Frenkel, B. Smit, Understanding Molecular Simulation: From Algorithms to Applications, Elsevier, 2001.

[25] A.P. Thompson, H.M. Aktulga, R. Berger, D.S. Bolintineanu, W.M. Brown, P.S. Crozier, P.J. in 't Veld, A. Kohlmeyer, S.G. Moore, T.D. Nguyen, R. Shan, M.J. Stevens, J. Tranchida, C. Trott, S.J. Plimpton, LAMMPS - a flexible simulation tool for particle-based materials modeling at the atomic, meso, and continuum scales, Comput. Phys. Commun. 271 (2022) 108171. https://doi.org/10.1016/j.cpc.2021.108171.

[26] R.T. Cygan, J.-J. Liang, A.G. Kalinichev, Molecular Models of Hydroxide, Oxyhydroxide, and Clay Phases and the Development of a General Force Field, J. Phys. Chem. B. 108 (2004) 1255–1266. https://doi.org/10.1021/jp0363287.

[27] A.C.T. van Duin, S. Dasgupta, F. Lorant, W.A. Goddard, ReaxFF: A Reactive Force Field for Hydrocarbons, J. Phys. Chem. A. 105 (2001) 9396–9409. https://doi.org/10.1021/jp004368u.

[28] S. Hajilar, B. Shafei, Mechanical failure mechanisms of hydrated products of tricalcium aluminate: A reactive molecular dynamics study, Mater. Des. 90 (2016) 165–176. https://doi.org/10.1016/j.matdes.2015.10.089.

[29] D. Hou, C. Wu, Q. Yang, W. Zhang, Z. Lu, P. Wang, J. Li, Q. Ding, Insights on the molecular structure evolution for tricalcium silicate and slag composite: From 29Si and 27Al NMR to molecular dynamics, Compos. Part B Eng. 202 (2020) 108401. https://doi.org/10.1016/j.compositesb.2020.108401.

[30] D. Hou, J. Yu, P. Wang, Molecular dynamics modeling of the structure, dynamics, energetics and mechanical properties of cement-polymer nanocomposite, Compos. Part B Eng. 162 (2019) 433–444. https://doi.org/10.1016/j.compositesb.2018.12.142.

[31] W. Sekkal, A. Zaoui, Enhancing the interfacial bond strength of cement nanocomposite with carbonate nanostructure, Compos. Part B Eng. 124 (2017) 111–119. https://doi.org/10.1016/j.compositesb.2017.05.057.

[32] L. Liu, A. Jaramillo-Botero, W.A. Goddard, H. Sun, Development of a ReaxFF Reactive Force Field for Ettringite and Study of its Mechanical Failure Modes

from Reactive Dynamics Simulations, J. Phys. Chem. A. 116 (2012) 3918–3925. https://doi.org/10.1021/jp210135j.

[33] Y. Liang, Mechanical and fracture properties of calcium silicate hydrate and calcium hydroxide composite from reactive molecular dynamics simulations, Chem. Phys. Lett. 761 (2020) 138117. https://doi.org/10.1016/j.cplett.2020.138117.

[34] P.A. Bonnaud, C. Labbez, R. Miura, A. Suzuki, N. Miyamoto, N. Hatakeyama, A. Miyamoto, K.J.V. Vliet, Interaction grand potential between calcium–silicate–hydrate nanoparticles at the molecular level, Nanoscale. 8 (2016) 4160–4172. https://doi.org/10.1039/C5NR08142D.

[35] X. Zhu, A. Zaoui, W. Sekkal, Wettability and work of adhesion of water nanodroplet on (001) surface of cement paste, Cem. Concr. Res. 159 (2022) 106896. https://doi.org/10.1016/j.cemconres.2022.106896.

[36] M. Eftekhari, S. Mohammadi, Molecular dynamics simulation of the nonlinear behavior of the CNT-reinforced calcium silicate hydrate (C–S–H) composite, Compos. Part Appl. Sci. Manuf. 82 (2016) 78–87. https://doi.org/10.1016/j.compositesa.2015.11.039.

[37] Z. Wu, E. Zhao, H. Xiang, X. Hao, X. Liu, J. Meng, Crystal structures and elastic properties of superhard Ir N2 and Ir N3 from first principles, Phys. Rev. B. 76 (2007) 054115. https://doi.org/10.1103/PhysRevB.76.054115.

[38] J. Fu, H. Bai, Z. Zhang, W. Lin, Elastic constants and homogenized moduli of manganese carbonate structure based on molecular dynamics and Reuss-Voigt-Hill methods, IOP Conf. Ser. Mater. Sci. Eng. 423 (2018) 012046. https://doi.org/10.1088/1757-899X/423/1/012046.

[39] S. Kamali, Comportement et simulation des matériaux cimentaires en environnement agressifs: lixiviation et température, PhD Thesis, Cachan, Ecole normale supérieure, 2003.

[40] F. Bernard, J. Fu, S. Kamali-Bernard, Multiscale modelling approach to determine the specific heat of cementitious materials, Eur. J. Environ. Civ. Eng. 23 (2019) 535–551. https://doi.org/10.1080/19648189.2018.1443157.

[41] J. Fu, F. Bernard, S. Kamali-Bernard, Assessment of the elastic properties of amorphous calcium silicates hydrates (I) and (II) structures by molecular dynamics simulation, Mol. Simul. 44 (2018) 285–299. https://doi.org/10.1080/08927022.2017.1373191.

[42] Y. Huang, Yong, B. Karami, D. Shahsavari, A. Tounsi, Static stability analysis of carbon nanotube reinforced polymeric composite doubly curved micro-shell panels, Archives of Civil and Mechanical Engineering 21 (4) (2021) article id.139. https://doi.org/ 10.1007/s43452-021-00291-7.

[43] P. Talebizadehsardari, A. Eyvazian, M. Asmael, B. Karami, D. Shahsavari, R.B. Mahani, Static bending analysis of functionally graded polymer composite curved beams reinforced with carbon nanotubes, Thin-Walled Structures 157 (2020) 107139. https://doi.org/10.1016/j.tws.2020.107139.

[44] A. Eyvazian, D. Shahsavari, B. Karami, On the dynamic of graphene reinforced nanocomposite cylindrical shells subjected to a moving harmonic load, International Journal of Engineering Science 154 (2020) 103339. https///doi.org/10.1016/j.ijengsci.2020.103339.

[45] B. Karami, D. Shahsavari, On the forced resonant vibration analysis of functionally graded polymer composite doubly-curved nanoshells reinforced with graphene-nanoplatelets, Comput. Methods Appl. Mech. Engrg. 359 (2020) 112767. https://doi.org/10.1016/j.cma.2019.112767.

Declaration of interests

☒ The authors declare that they have no known competing financial interests or personal relationships that could have appeared to influence the work reported in this paper.

☐ The authors declare the following financial interests/personal relationships which may be considered as potential competing interests:

Graphical abstract